Adaptive Resonant Beam Charging for Intelligent Wireless Power Transfer

Qingqing Zhang, *Student Member, IEEE*, Wen Fang, Mingliang Xiong, Qingwen Liu, *Senior Member, IEEE*, Jun Wu, *Senior Member, IEEE*, and Pengfei Xia

***Abstract*—As a long-range high-power wireless power transfer (WPT) technology, resonant beam charging (RBC) can transmit watt-level power over long distance for the devices in the Internet of Things (IoT). Due to its open-loop architecture, RBC faces the challenge of providing dynamic current and voltage to optimize battery charging performance. In RBC, battery overcharge may cause energy waste, thermal effects, and even safety issues. On the other hand, battery undercharge may lead to charging time extension and significant battery capacity reduction. In this paper, we present an adaptive RBC (ARBC) system for battery charging optimization. Based on RBC, ARBC uses a feedback system to control the supplied power dynamically according to the battery preferred charging values. Moreover, in order to transform the received current and voltage to match the battery preferred charging values, ARBC adopts a dc–dc conversion circuit. Relying on the analytical models for RBC power transmission, we obtain the end-to-end power transfer relationship in the approximate linear closed-form of ARBC. Thus, the battery preferred charging power at the receiver can be mapped to the supplied power at the transmitter for feedback control. Numerical evaluation demonstrates that ARBC can save 61% battery charging energy and 53%–60% supplied energy compared with RBC. Furthermore, ARBC has high energy-saving gain over RBC when the WPT is unefficient. ARBC in WPT is similar to link adaption in wireless communications. Both of them play the important roles in their respective areas.**

***Index Terms*—Wireless power transfer (WPT).**

I. Introduction

INTERNET of Things (IoT) takes significant strides and has become the driving force of scientific revolution and industrial transformation [1]. However, IoT development faces the challenge of device power endurance. Meanwhile, dramatic growth of the multimedia process in mobile devices leads to significant energy consumption [2], [3]. Carrying a power cord and looking for power supply cause inconvenience for users. Hence, wireless power transfer (WPT) technology becomes an attractive solution for the power hunger [4]–[6].

Manuscript received April 23, 2018; revised July 28, 2018; accepted August 25, 2018. Date of publication August 29, 2018; date of current version February 25, 2019. The material in this paper was presented in part at the 2017 IEEE 86th Vehicular Technology Conference (VTC2017-Fall), Toronto, ON, Canada, September 24–27, 2017. *(Corresponding author: Qingwen Liu.)*

The authors are with the Department of Computer Science and Technology, Tongji University, Shanghai 201800, China (e-mail: anne@tongji.edu.cn; wen.fang@tongji.edu.cn; xiongml@tongji.edu.cn; qliu@tongji.edu.cn; wujun@tongji.edu.cn; pengfei.xia@gmail.com).

Digital Object Identifier 10.1109/JIOT.2018.2867457

To provide perpetual power supply for mobile devices, WPT should provide high power over long distance. The existing WPT technologies include inductive coupling, magnetic resonance, radio frequency and laser. However, the transmission distances of inductive coupling and magnetic resonance are only within millimeter or centimeter, which cannot support long distance WPT [7], [8]. Radio frequency and laser are unsafe when transmitting watt-level power [9], [10].

To support watt-level power transmission over meter-level distance safely, Wi-Charge has published the wireless power delivery products and has received the FDA safety approval [11]. The Wi-Charge transmitter can deliver up to 3 W power over 5 m to multiple receivers simultaneously through infrared beams while guaranteeing the safety and mobility [11], [12]. The resonant beam charging (RBC), i.e., distributed laser charging, was at first presented in [13].

The RBC mechanism, mathematical models and features are depicted in [14] and [15]. The self-aligning feature of RBC provides users a convenient way to charge their devices without specific aiming or tracking, as long as the transmitter and the receiver are in the line-of-sight (LOS) of each other. RBC supports charging multidevice simultaneously, which is like multi WiFi-devices connecting to a single access point [11], [14], [15]. Additionally, once there is an obstacle between the RBC transmitter and receiver, WPT can be cut off right away. Therefore, the RBC system guarantees safety.

On the other hand, to keep all IoT devices accessing to the RBC system working as long as possible for fairness, the first access first charge scheduling algorithm was presented in [16]. Multidevice can be selected to charge with their batteries' preferred charging power according to the accessing order, while all receivers discharge depending on their using statues during a time slot.

As smart-home has become an important IoT application area, Fig. 1 gives an example of RBC application in an indoor scenario. In Fig. 1, the ceiling light is the RBC-equipped light bulb, where an RBC transmitter is embedded in. All the electronic devices embedded with the RBC receivers in the coverage of the RBC transmitter can be charged wirelessly and simultaneously.

However, the preferred charging current, voltage, and thus power of battery, such as the most widely used Li-ion battery, keep changing during the charging period [17], [18]. If the transmitter could adjust the emitted power according to the battery preferred value, battery charging performance, and WPT efficiency can be optimized. To this end, an adaptive

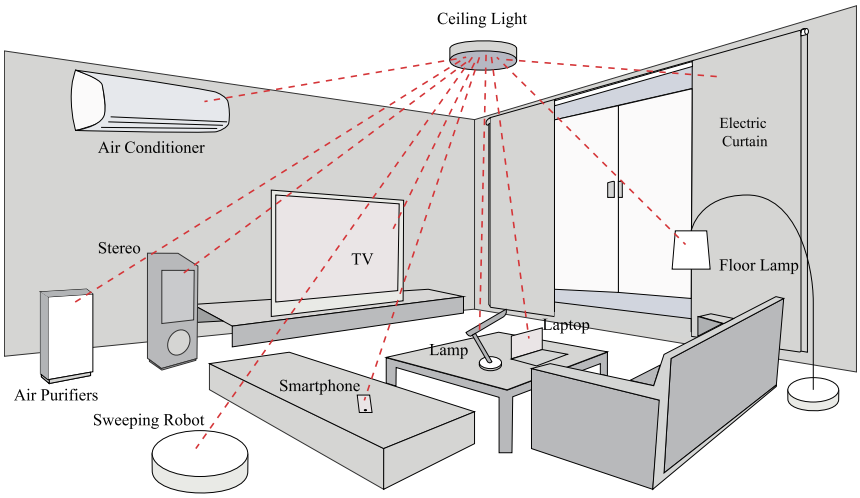

Fig. 1. Example application scenario.

RBC (ARBC) system based on the RBC system is introduced in this paper.

The contributions of this paper can be summarized as follows.

1) We propose the ARBC system design, which can automatically adjust the resonant beam power relying on the feedback control.
2) We illustrate the working flow, create the mathematical model, and present the control algorithm of the ARBC system, which provide the guidelines for the ARBC system implementation.
3) We analyze the ARBC system performance considering various conditions including beam wavelength, PV-cell temperature, air quality, etc. We find 61% battery charging energy and 53%–60% supplied energy can be saved by the ARBC system compared with the RBC system.

In this paper, RBC will be briefly introduced at first. Then, we will introduce the ARBC system. The modules and working mechanisms of the ARBC system will be depicted in the following. The ARBC system design, including the mathematical modeling and the control algorithm, will be presented to quantitatively analyze the ARBC model. Based on the system design, we will evaluate the system performance by using MATLAB and Simulink. Finally, the conclusions will be given and the open issues for future research will be discussed.

II. System Architecture

In this section, we will briefly introduce the RBC system at first [13]. Then, we will propose the ARBC system based on the RBC system.

A. RBC System

Fig. 2 shows the RBC system, where the transmitter and the receiver are separated in space. A power supply, a retro-reflector R1 with 100% reflectivity and a gain medium, which is used to amplify photons, are included in the RBC transmitter. While in the RBC receiver, a retro-reflector R2 with 95%

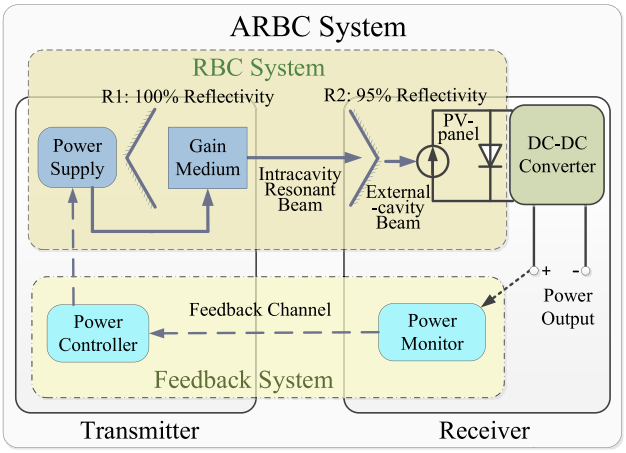

Fig. 2. ARBC system diagram.

reflectivity is contained. A photoelectric conversion component, such as photovoltaic-panel (PV-panel), is installed behind R2 at the receiver.

In the RBC system, the electrical power provided by the power supply is converted to the intracavity resonant beam power. Then, the intracavity resonant beam travels through the air from the transmitter to the receiver with certain attenuation. At the receiver, the intracavity resonant beam can be partially converted to the external-cavity beam after passing through R2. Then, the PV-panel converts the external-cavity beam power to the electrical power. Thus, batteries can be charged by the electrical power.

1) Electricity-to-Beam Conversion: The power supply provides electrical power P_s to pump the gain medium. P_s depends on the stimulating current I_t and voltage V_t as

$$P_s = I_t V_t. \tag{1}$$

Then, the intracavity resonant beam can be stimulated out from the gain medium. If there is no transmission attenuation, the external-cavity resonant beam power at the receiver P_{bt}

can be derived as [19]

$$P_{\rm bt} = \gamma \frac{h\nu}{q}(I_t - I_{\rm th}) \tag{2}$$

where γ is the modified coefficient, h is the Plunk constant, ν is the beam frequency, q is the electronic charge constant, and $I_{\rm th}$ is the current threshold.

2) Beam Transmission: The intracavity resonant beam travels through the air and arrives at the RBC receiver. During the transmission, the beam power suffers from attenuation, which is similar to electromagnetic wave propagation power loss [20].

The beam transmission efficiency $\eta_{\rm bt}$ can be modeled as [21]

$$\eta_{\rm bt} = \frac{P_{\rm br}}{P_{\rm bt}} = e^{-\sigma R} \tag{3}$$

where $P_{\rm br}$ is the received external-cavity beam power at the receiver, σ is the beam attenuation coefficient, and R is the transmission radius. When R is close to zero, $\eta_{\rm bt}$ approaches 100%, and thus $P_{\rm br}$ is approximate to $P_{\rm bt}$.

3) Beam-to-Electricity Conversion: At the receiver, the external-cavity beam power $P_{\rm br}$ can be received by a PV-panel and then be converted to electrical power [22], [23]. The relationship between the PV-panel output current $I_{o,\rm pv}$ and voltage $V_{o,\rm pv}$ can be depicted as

$$I_{o,\rm pv} = I_{sc} - I_s\left(e^{V_{o,\rm pv}/V_m} - 1\right) \tag{4}$$

where I_{sc} is the PV-panel short-circuit current, and I_s is the saturation current, i.e., the diode leakage current density in the absence of light. V_m is the "thermal voltage," which can be defined as

$$V_m = \frac{nkT}{q} \tag{5}$$

where n is the PV-panel ideality factor, k is the Boltzmann constant, and T is the PV-cell temperature. Then, the PV-panel output power $P_{o,\rm pv}$ can be obtained as

$$P_{o,\rm pv} = I_{o,\rm pv} V_{o,\rm pv}. \tag{6}$$

In the RBC system, the electrical power $P_{o,\rm pv}$ can finally be used to charge batteries.

B. ARBC System

The RBC system can transmit watt-level power over long distance [13]. However, there exist some concerns with the RBC system.

1) To optimize battery charging performance, the battery charging current and voltage should be dynamically changed during the charging period, which will be discussed in detail in the following. However, the RBC system can only charge batteries with constant current and voltage.
2) The RBC resonant beam power propagation loss depends on transmission radius and medium obstacle along the LOS path between the transmitter and the receiver [13]. Thus, the space-time varying propagation loss requires dynamic power supply compensation.
3) If the PV-panel output power at the RBC receiver is not fully converted to the battery power, the extra energy usually causes thermal effects, which may lead to PV-panel conversion efficiency reduction, battery damage, and even danger.

To deal with these issues, an intuitive idea is to control the transmission power by adaptively sending the value of battery preferred power from the receiver to the transmitter through a feedback channel. The similar mechanism for signal transmission is well-known as link adaption in wireless communication for optimizing the information delivery [24].

At first, we need to specify the adaption goal to optimize battery charging performance. Battery charging profile is the algorithm of using dynamic current and voltage in battery charging process. Battery performance, in terms of achievable capacity and charging speed, depends on the battery charging profile. For example, the preferred battery charging profile of Li-ion battery is known as the constant current–constant voltage (CC–CV) profile to achieve the maximum battery capacity [18].

On the other hand, the PV-panel output current and voltage may not be the battery preferred charging values, the dc–dc converter can take the role of converting the PV-panel output values to the battery preferred ones.

By incorporating the feedback system and the dc–dc converter into the RBC system, the ARBC system architecture can be depicted as in Fig. 2. The feedback system crosses over the two ends of the ARBC system, which consists of power monitor and power controller.

The ARBC operation flow is depicted in Fig. 3 as follows.

1) The power monitor gets the values of battery preferred charging current, voltage, and cut-off time.
2) If the preferred charging current is lower than 20 mA, the charging procedure ends. Or, turn to 3).
3) If the charging time cuts off, the charging procedure ends. Or, turn to 4).
4) The power monitor sends the preferred charging power to the power controller.
5) After receiving the preferred charging values, the power controller informs the power supply to generate the corresponding electrical power. The electrical power has effects on the gain medium to stimulate out the intracavity resonant beam.
6) The resonant beam travels through the air from the transmitter and arrives at the receiver.
7) The receiver beam power is converted to the electrical power by the PV-panel at the receiver.
8) The dc–dc converter converts the PV-panel output current and voltage to the battery preferred values.
9) The battery is charged with the preferred current and voltage.
10) The power monitor updates the values of battery preferred charging current, voltage, and cut-off time according to the battery status.

Repeating this flow, the battery can be charged with the preferred values during the whole charging procedure.

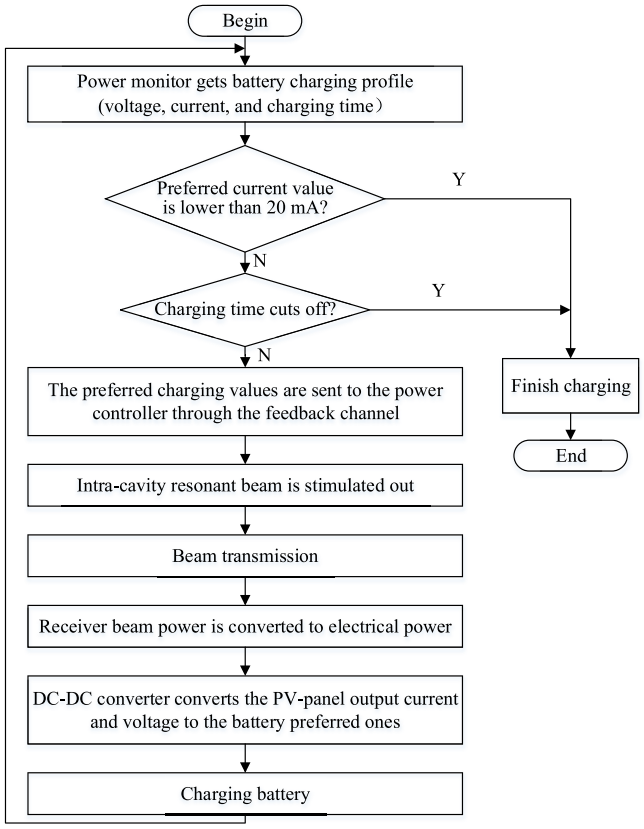

Fig. 3. ARBC flow chart.

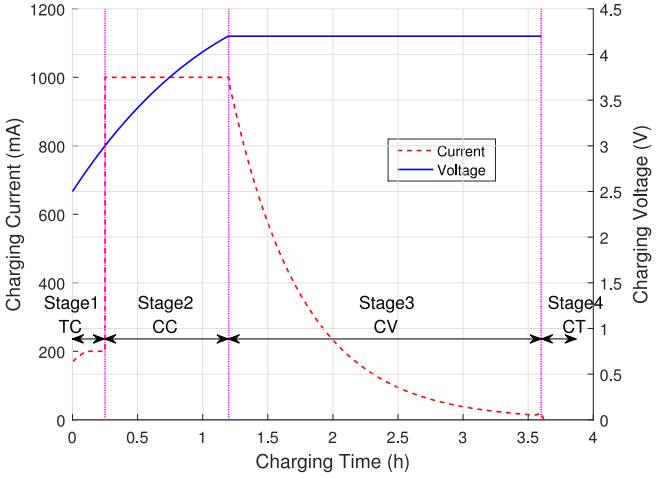

Fig. 4. Li-ion battery charging profile.

To specify the ARBC system in detail, the battery charging profile, the dc–dc converter and the feedback mechanism is discussed in the following.

1) Li-Ion Battery Charging Profile: Different kinds of batteries may have different charging profiles given the chemical characteristics [25]. Li-ion battery is the most widely used rechargeable battery for IoT and mobile devices. In traditional charging systems, including the RBC system, batteries are charged with fixed power. However, for Li-ion battery, even slightly undercharging can lead to significant capacity reduction [26]. For example, 1.2% undercharge of the optimal full-charge voltage may result in 9% capacity reduction. On the other hand, overcharge may damage the battery and even cause danger. Therefore, offering controllable current and voltage is important to charge Li-ion battery safely, as well as achieve its full capacity.

We discuss here the Li-ion battery preferred charging profile, which includes four stages as in Fig. 4. As an instance of a single cell Li-ion battery with 1000 mAh capacity, the battery can theoretically provide 1 h of operating time when discharged at a constant current of 1000 mA. We outline the stages of battery charging profile as [26] and [27]:

Stage 1 [Trickle Charge (TC)]: When the battery voltage is below 3.0 V, the battery is charged with the current which increases toward 200 mA. The voltage rises to 3.0 V.

Stage 2 [Constant Current (CC) Charge]: After the battery voltage has risen above 3.0 V, the TC–CC threshold, the charging current switches to constant value between 200 to 1000 mA. The voltage rises toward 4.2 V.

Stage 3 [Constant Voltage (CV) Charge]: When the cell voltage reaches the CC–CV threshold, 4.2 V, the CC stage ends and the CV stage begins. In order to maximize capacity, the voltage variation tolerance should be less than 1%. The current decreases toward 20 mA.

Stage 4 (Charge Termination): Two approaches are typically used to terminate charging: 1) minimum current charge or 2) timer cutoff. However, a combination of the two techniques may also be applied. In the minimum current approach, battery charge is terminated, when the current diminishes below 20 mA, the minimum current threshold, during the CV stage. In the timer cutoff approach, for example, 2.4-h timer starts when the CV stage is invoked. The charge is terminated after 3.6-h during the CV stage.

It takes 4 h to fully charge a deeply depleted battery to maximize the battery capacity. The charging speed is affected by CC in Stage 2 [18]. For example, if CC is 700 mA, 50%–70% capacity can be charged at the end of Stage 2. This is the secret that many "fast-charging" techniques rely on. If CC is 200 mA, much longer time is needed to finish Stage 2, however, nearly 100% capacity can be achieved at the end of Stage 2. It is the tradeoff between charging speed and achieved capacity, which can be controlled by CC at Stage 2.

Compared with fixed-charging system, dynamically charging, according to the above charging profile, can not only avoid overcharge or undercharge, but also reduce potential damage to battery or safety concern.

2) DC–DC Conversion: The PV-panel output current $I_{o,\mathrm{pv}}$ and voltage $V_{o,\mathrm{pv}}$ may not be optimal for battery charging. At first, $I_{o,\mathrm{pv}}$ and $V_{o,\mathrm{pv}}$ may be dynamic due to the variance of P_{br} and PV-panel characteristics. Second, the preferred battery charging current and voltage vary with different battery conditions, as discussed above. Therefore, converting $I_{o,\mathrm{pv}}$ and $V_{o,\mathrm{pv}}$ to the battery preferred values becomes imperative.

In solar power systems, it is well-known to adopt a dc–dc converter between PV-panel and power load to obtain the preferred current and voltage [28]. There are three dc–dc converter types: 1) boost converter; 2) buck converter; and 3) buck-boost converter. At the ARBC receiver, the buck-boost converter is adopted [29]. As depicted in Fig. 5, the dc–dc

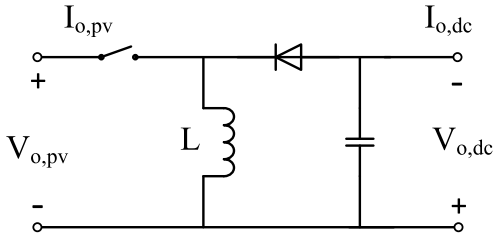

Fig. 5. Buck-boost dc–dc converter.

converter, a programmable integrated circuit, can convert the input current and voltage, which are the PV-panel output current $I_{o,\mathrm{pv}}$ and voltage $V_{o,\mathrm{pv}}$, to the output current $I_{o,\mathrm{dc}}$ and voltage $V_{o,\mathrm{dc}}$, which are the battery preferred charging current and voltage.

There are two working modes of the buck-boost dc–dc converter according to whether the current through the inductor falls to zero during a working period. If the current through the inductor never falls to zero, it is called the continuous mode. Otherwise, it is the discontinuous mode.

When working at the continuous mode, the relationship between $V_{o,\mathrm{pv}}$ and $V_{o,\mathrm{dc}}$ can be depicted as

$$\frac{V_{o,\mathrm{dc}}}{V_{o,\mathrm{pv}}} = -\frac{D}{1-D} \tag{7}$$

where D is the duty cycle, which means the switch closing time of the whole working time t. While, if working at the discontinuous mode, $V_{o,\mathrm{pv}}$ and $V_{o,\mathrm{dc}}$ are related as

$$\frac{V_{o,\mathrm{dc}}}{V_{o,\mathrm{pv}}} = -\frac{V_{o,\mathrm{pv}} D^2\ t}{2\ L\ I_{o,\mathrm{pv}}} \tag{8}$$

where L is the inductor.

Then, the dc–dc converter output current and voltage are converted to the battery preferred charging current and voltage. Thus, batteries can be charged with the preferred values.

3) Feedback Mechanism: To charge batteries dynamically and continuously, we should track the preferred battery charging current, voltage, and thus power, and send the information to the power supply during the charging procedure. In the feedback system, the power monitor at the ARBC receiver takes the role of tracking the battery status and obtaining the charging values of current and voltage. After that, the expected charging power can be calculated as the product of the preferred current and voltage.

Then, the adjustment or requirement of the transmitting power will be sent to the power controller by the power monitor through the feedback channel. The feedback channel can be established relying on various wireless communication technologies, e.g., WiFi, Bluetooth, infra-communication. Alternatively, the decision logic can be implemented in the power controller, if the power monitor can feedback the battery charging related information to the power controller.

Thus, the battery can be charged with preferred current and voltage continuously. Thereafter, the intelligent wireless charging technology can be realized to optimize battery performance. This architecture is capable to support charging different kinds of batteries with diverse charging profiles, such as Li-ion, Ni-MH, etc.

TABLE I
CURVE-FITTING COEFFICIENTS FOR BEAM POWER

Beam Wavelength	a_1	b_1
810 nm	0.445	-0.75
1550 nm	0.34	-1.1

TABLE II
BEAM TRANSMISSION PARAMETERS

Parameter	Value		
	Clear Air	**Haze**	**Fog**
τ	$10\ km$	$3\ km$	$0.4\ km$
θ	1.3	$0.16\tau + 0.34$	0

In summary, the proposed ARBC mechanism for optimizing wireless charging performance is similar to the link adaption widely used in wireless communications for optimizing information delivery.

In the next section, we will present the numerical models and performance evaluation of the ARBC system.

III. ARBC SYSTEM DESIGN

To design the ARBC system, the power relationship between the battery preferred charging power and the supplied power should be obtained. So, we will introduce the numerical models at first in this section. Based on these models, we will design the system control algorithm to describe the ARBC system in detail.

A. Mathematical Modeling

We at first introduce the electricity-to-beam conversion model, the beam transmission model, and the beam-to-electricity conversion model. Based on these models, the ARBC end-to-end power transfer relationship between the battery power and the supplied power can be obtained, which offers a quantitative and intuitive tool to evaluate the ARBC system.

1) Electricity-to-Beam Conversion: From [30] and [31], the measured values of stimulation current I_t, stimulation voltage V_t, and the resonant beam power P_{bt} for the beam wavelength of 810 and 1550 nm can be obtained, respectively. Then, the supplied electrical power P_s can be calculated according to (1). According to [14] and [15], P_s is verified to be linearly related with P_{bt}. The relationship between P_{bt} and P_s can be described as

$$P_{\mathrm{bt}} \approx a_1 P_s + b_1 \tag{9}$$

where a_1 and b_1 are two coefficients, of which the values are listed in Table I.

In Fig. 6, the dotted-dashed-line and the dotted-line depict the measured relationships between P_{bt} and P_s when the beam wavelength takes 810 and 1550 nm, respectively. While, the solid-line and the dashed-line are the formulated fitting curves for 810 and 1550 nm based on (9). As can be seen, the formulated curves match the measured ones very well, which validates the linear approximation.

2) Beam Transmission: In different transmission scenarios, the intracavity resonant beam power takes different attenuation

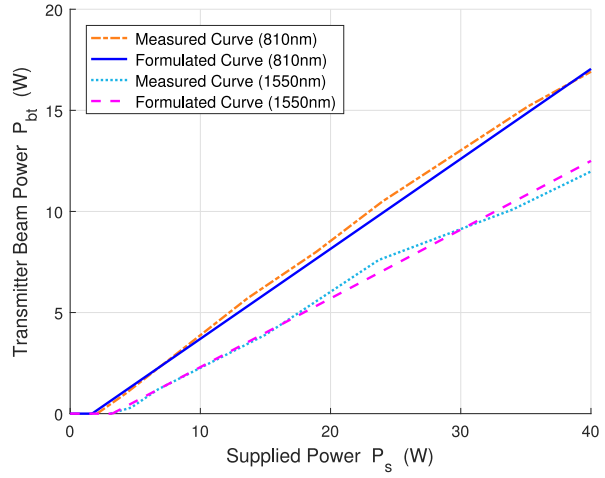

Fig. 6. Transmitter beam power versus supplied power.

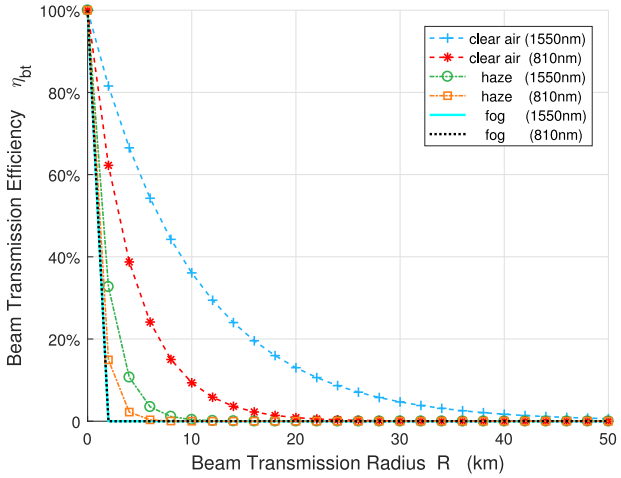

Fig. 7. Beam transmission efficiency versus radius.

according to (3). The attenuation coefficient σ can be depicted as [21]

$$\sigma = \frac{3.91}{\tau}\left(\frac{\lambda}{550\ \text{nm}}\right)^{-\theta} \tag{10}$$

where τ is the visibility, and θ is the size distribution of the scattering particles.

We consider three typical scenarios, i.e., clear air, haze, and fog here. θ can be specified as [32]

$$\theta = \begin{cases} 1.3, & \text{for clear air} \quad (6\ \text{km} \le \tau \le 50\ \text{km}) \\ 0.16\tau + 0.34, & \text{for haze} \quad (1\ \text{km} \le \tau \le 6\ \text{km}) \\ 0, & \text{for fog} \quad (\tau \le 0.5\ \text{km}). \end{cases} \tag{11}$$

These transmission parameters are listed in Table II.

Fig. 7 illustrates how η_{bt} varies with the transmission radius R under three different air quality and two different beam wavelengths. We can see that, η_{bt} decays exponentially with the increment of R. Meanwhile, for the same beam wavelength, η_{bt} has much steeper shape with the decrement of τ. It means that η_{bt} declines faster with the air quality declining, i.e., the visibility gets low.

TABLE III
PV-PANEL SIMULATION PARAMETERS

Parameter	Value	
	810 nm	1550 nm
Short-circuit current	$0.16732A$	$0.305A$
Open-circuit voltage	$1.2V$	$0.464V$
Irradiance used for measurement	$36.5W/cm^2$	$2.7187W/cm^2$
Laser frequency	$3.7037 \times 10^{14}Hz$	$1.9355 \times 10^{14}Hz$
Quality factor	1.5	1.1
Number of series cells	72	
PV-panel material	GaAs-based	GaSb-based
Measurement temperature	$25°C$	$120°C$

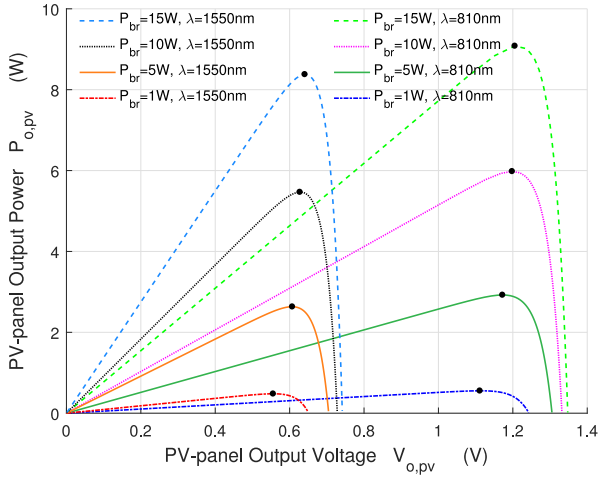

Fig. 8. PV-panel output power versus voltage (25 °C).

In addition, in the clear air and the haze scenarios, given the same radius R, the beam power attenuates faster for the short beam wavelength. When θ takes 0 in the fog scenario, for 810 and 1550 nm, η_{bt} has the same attenuation pattern.

3) Beam-to-Electricity Conversion: At the ARBC receiver, various factors like the input beam power P_{br}, the beam wavelength λ, and the PV-cell temperature T affect the PV-panel power conversion. We simulate the beam-to-electricity conversion procedure with the standard solar cell Simulink model [15]. Table III lists all the simulation parameters.

When the PV-cell temperature T is 25 °C (298K), Fig. 8 illustrates the influences that P_{br} and λ have on the PV-panel output power $P_{o,\text{pv}}$ based on (4)–(6).

From Fig. 8, $P_{o,\text{pv}}$ goes up gradually to the peak and then declines sharply to the bottom. The PV-panel outputs more power with the increment of P_{br}. The dots in Fig. 8 are the maximum power points (MPPs) of the curves, which have been proved that uniquely exist [33]. Similarly, the MPPs when T takes 0 °C (273K) and 50 °C (323K) can be obtained.

To obtain the maximum efficiency of the ARBC system, the PV-panel is expected to work at MPPs. Moreover, the maximum $P_{o,\text{pv}}$ should be the preferred battery charging power P_b. The dots in Fig. 9 are the MPPs obtained under different PV-cell temperatures (0 °C, 25 °C, and 50 °C) and beam wavelengths (810 and 1550 nm). From Fig. 9, the relationship between P_b and P_{br} can be obtained by the linear curve-fitting

TABLE IV
CURVE-FITTING COEFFICIENTS FOR BATTERY POWER

Beam Wavelength	Temperature	a_2	b_2
810 nm	0°C	0.6084	-0.08382
	5°C	0.6087	-0.08506
	10°C	0.6089	-0.08628
	15°C	0.6092	-0.08749
	20°C	0.6094	-0.08868
	25°C	0.6096	-0.08987
	30°C	0.6098	-0.09102
	35°C	0.6100	-0.09217
	40°C	0.6102	-0.09331
	45°C	0.6103	-0.09443
	50°C	0.6105	-0.09557
1550 nm	0°C	0.6043	-0.1275
	5°C	0.5964	-0.1294
	10°C	0.5885	-0.1317
	15°C	0.5806	-0.1338
	20°C	0.5727	-0.1358
	25°C	0.5649	-0.1382
	30°C	0.5569	-0.1398
	35°C	0.5491	-0.1424
	40°C	0.5412	-0.1440
	45°C	0.5334	-0.1464
	50°C	0.5255	-0.1483

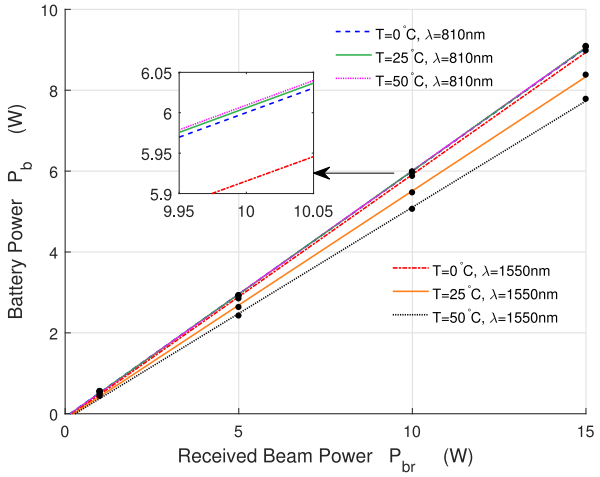

Fig. 9. Battery power versus received beam power.

approximation as [14], [15]

$$P_b \approx a_2 P_{\text{br}} + b_2 \tag{12}$$

where a_2 and b_2 are the linear curve fitting coefficients. To provide more details about how P_b changes with P_{br} under different temperature, values of a_2 and b_2 when the PV-cell temperature takes 0 °C, 5 °C, 10 °C, 15 °C, 20 °C, 25 °C, 30 °C, 35 °C, 40 °C, 45 °C, and 50 °C are listed in Table IV.

Fig. 9 depicts the linear relationship between P_b and P_{br} for 810 and 1550 nm, respectively. The linear fitting lines match the measured P_b and P_{br}, which are marked by the dots, very well. With the increment of T, for same P_{br}, the value of P_b diminishes. On the other hand, the 1550 nm system is more temperature-dependent than the 810 nm system.

4) End-to-End Transmission: Efficiency of battery charging, dc–dc conversion and feedback affect the end-to-end power transmission efficiency. We can assume there is almost no energy loss if the battery is charged with preferred power values. We also assume that the feedback system and the dc–dc converter cause almost no energy loss [34]. Thus, the ARBC end-to-end power transmission mathematical model can be built based on the numerical models.

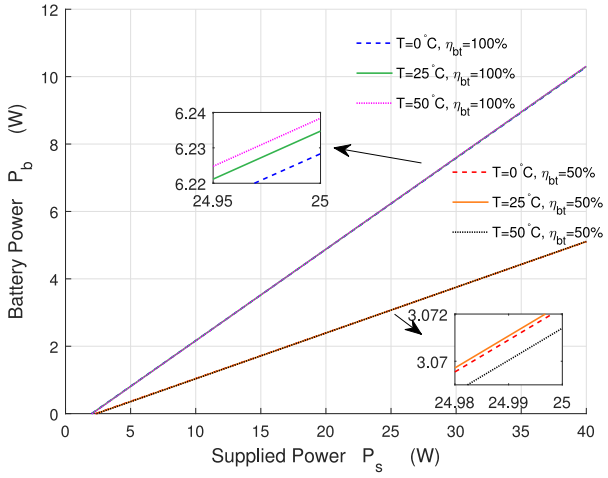

Fig. 10. Battery power versus supplied power (810 nm).

Algorithm 1 ARBC

Begin
The power monitor gets the preferred charging power P_b, current I_b, voltage V_b and cut-off time t
while $I_b \geq 20$ mA **and** $t \leq 3.6$ h **do**
  $P_s \leftarrow P_b/(\eta_{eb}\eta_{bt}\eta_{pv})$ // The power monitor computes P_s, and sends it to the power controller
  $P_{bt} \leftarrow P_s\eta_{eb}$ // Transmitter beam power
  $P_{br} \leftarrow P_{bt}\eta_{bt}$ // Receiver beam power
  $P_b \leftarrow P_{br}\eta_{pv}$ // PV-panel output power
  if $I_{pv} \neq I_b$ **and** $V_{pv} \neq V_b$ **then** // DC-DC conversion
    $I_b \leftarrow I_{pv}$
    $V_b \rightarrow V_{pv}$
  end if
  Charge the battery with I_b and V_b
  The power monitor updates P_b, I_b and V_b according to the next battery state
end while
Stop Charging
End

Based on (3), (9), and (12), given the beam transmission efficiency η_{bt}, the battery charging power P_b changes depending on the supplied power P_s as

$$P_b \approx a_2\eta_{\text{bt}}P_{\text{bt}} + b_2 = a_1a_2\eta_{\text{bt}}P_s + (a_2b_1\eta_{\text{bt}} + b_2). \tag{13}$$

Hence, P_b depends on P_s linearly. For the 810 nm system, Fig. 10 depicts the linear relationship under three different T when η_{bt} takes 100% and 50%, respectively. While, Fig. 11 depicts the same relationships for the 1550 nm system.

The linear relationship between P_b and P_s provides an intuitive and quantitive way to understand the end-to-end power transfer in the ARBC system.

TABLE V
SUPPLIED ENERGY CONSUMPTION IN DIFFERENT SCENARIOS (Wh)

	Temperature T		0°C			25°C			50°C		
	Distance R		0.1 KM	0.5 KM	1 KM	0.1 KM	0.5 KM	1 KM	0.1 KM	0.5 KM	1 KM
810 nm	**RBC**	**Clear air**	64.20	69.91	77.86	64.15	69.85	77.79	64.15	69.86	77.80
		Haze	68.46	97.02	152.01	68.39	96.93	151.86	68.40	96.94	151.88
		Fog	156.23	7.59×10^3	1.0115×10^6	156.08	7.579×10^3	1.0105×10^6	156.09	7.58×10^3	1.0106×10^6
810 nm	**ARBC**	**Clear air**	29.97	32.28	35.49	29.99	32.31	35.52	30.05	32.36	35.58
		Haze	31.69	43.23	65.45	31.72	43.27	65.51	31.77	43.35	65.63
		Fog	67.15	3.069×10^3	4.087×10^5	67.22	3.073×10^3	4.091×10^5	67.34	3.079×10^3	4.099×10^5
1550 nm	**RBC**	**Clear air**	65.15	70.96	79.03	69.40	75.63	84.30	74.24	80.94	90.28
		Haze	69.47	98.51	154.40	74.04	105.19	165.15	79.23	112.78	177.37
		Fog	158.69	7.71×10^3	1.03×10^6	169.75	8.27×10^3	1.10×10^6	182.33	8.91×10^3	1.19×10^6
1550 nm	**ARBC**	**Clear air**	30.71	33.09	36.41	32.55	35.11	38.68	34.63	37.40	41.26
		Haze	32.48	44.39	67.31	34.46	47.28	71.96	36.69	50.55	77.22
		Fog	69.07	3.17×10^3	4.22×10^5	73.85	3.41×10^3	4.54×10^5	79.27	3.68×10^3	4.91×10^5

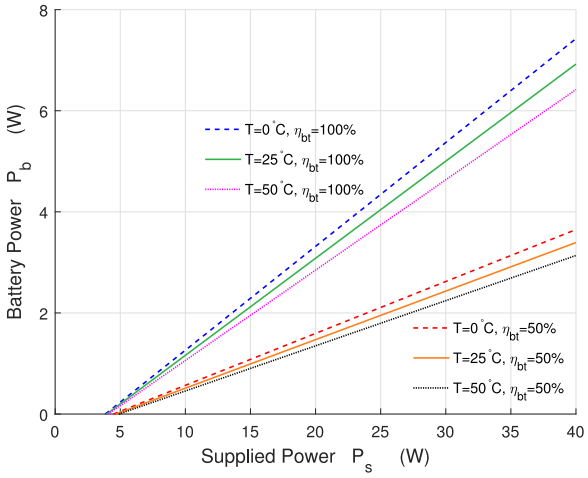

Fig. 11. Battery power versus supplied power (1550 nm).

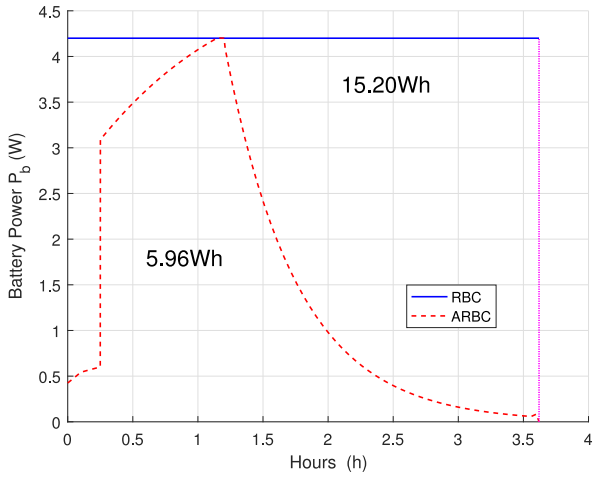

Fig. 12. Battery power in ARBC and RBC.

B. Control Algorithm

Based on the mathematical modeling, given the battery preferred charging current, voltage, and thus power, the supplied power can be calculated out with reference to the end-to-end transmission efficiency. To demonstrate the charging operation of the ARBC system, we give the charging algorithm in Algorithm 1 as follows.

1) The power controller gets the battery preferred charging power P_b, current I_b, voltage V_b, or cut-off time t from the power monitor.
2) If I_b is lower than 20 mA or t equals to 3.6 h, the charging procedure ends. Otherwise, the power controller informs the power supply to generate P_s from P_b with reference to the end-to-end transmission efficiency.
3) P_s effects on the gain medium, and the resonant beam can be stimulated out.
4) The PV-panel can convert the beam power to the electrical power P_{pv}, while the output current and voltage are I_{pv} and V_{pv}.
5) The dc–dc converter converts I_{pv} and V_{pv} to I_b and V_b. Thus, the battery can be charged with preferred values.
6) The power monitor updates I_b and V_b according to the next battery state, and sends them to the power controller. Then, turn to 2).

Repeating these steps, the battery can be charged with the battery preferred charging values dynamically during the whole ARBC procedure.

IV. PERFORMANCE EVALUATION

Based on the ARBC system design, the batteries accessed to the ARBC system can be charged with their preferred values. Therefore, the system performance can be evaluated. In terms of battery charging and power supply, the advantages of the ARBC system over the RBC system will be validated by the performance comparisons in this section. The numerical evaluations are implemented in MATLAB and Simulink.

A. Battery Charging Performance

In traditional wireless charging systems, including the RBC system, charging stages cannot be tracked without adaptive function. Hence, batteries are charged with fixed current or voltage. We take 4.2 W (constant current 1 A and constant voltage 4.2 V) for Li-ion battery charging power. The solid-line in Fig. 12 shows the constant battery charging power. It is an horizontal line without any changes during the RBC procedure.

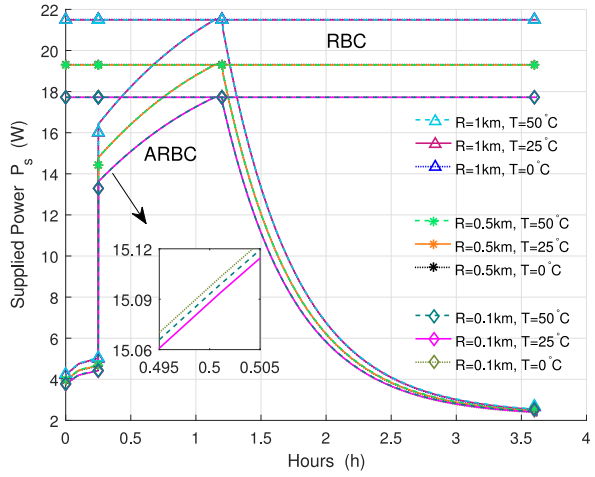

Fig. 13. Supplied power with different radius and temperature for 810 nm (clear air).

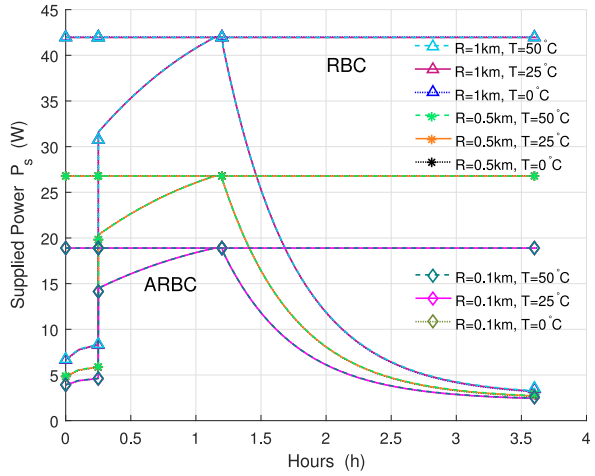

Fig. 14. Supplied power with different radius and temperature for 810 nm (haze).

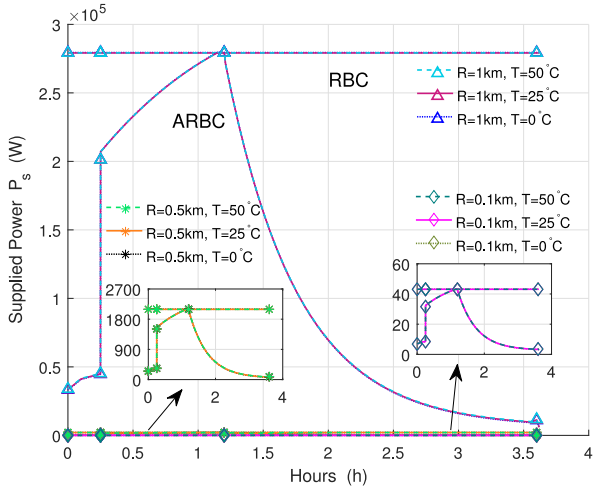

Fig. 15. Supplied power with different radius and temperature for 810 nm (fog).

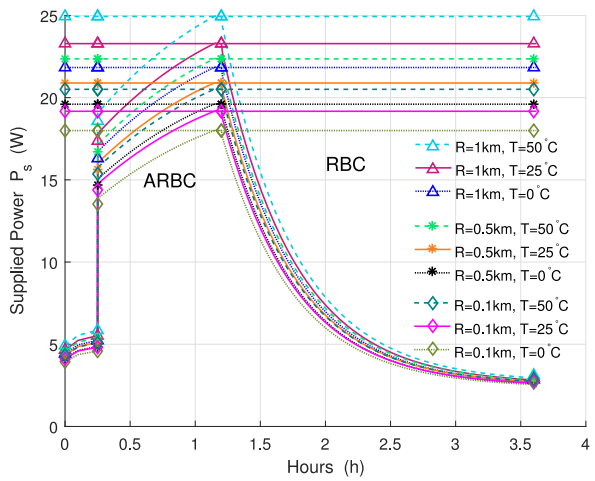

Fig. 16. Supplied power with different radius and temperature for 1550 nm (clear air).

However, batteries can be charged dynamically in the ARBC system. According to the Li-ion battery charging profile in Fig. 4, the preferred battery charging power can be obtained according to the preferred charging current and voltage. The dashed-line in Fig. 12 shows the preferred battery charging power changes during the ARBC procedure.

From Fig. 12, we can recognize the big power consumption gap between the RBC system and the ARBC system. The areas under the battery charging power in Fig. 12 stand for the consumed battery charging energy. The RBC procedure consumed energy is 15.20 Wh, while the ARBC procedure only consumes 5.96 Wh. That is, to say, during the whole charging procedure, the ARBC system could save 9.24 Wh energy. In summary, 61% battery charging energy can be saved by the ARBC system compared with the RBC system.

B. Power Supply Performance

For different transmission radius R, air quality, beam wavelength λ, and PV-cell temperature T, the supplied power P_s takes different values in the ARBC system. That is, P_s depends on R, T, λ and air quality. For $\lambda = 810$ nm, Figs. 13–15 show how P_s changes with different radius R under different air quality (clear air, haze, and fog) and different temperature T (0 °C, 25 °C, and 50 °C), respectively. Figs. 16–18 illustrate P_s in the same scenarios for $\lambda = 1550$ nm, respectively.

Form Figs. 13–18, when R increases, η_{bt} becomes small. Thus, P_s needs to be enhanced to compensate the power attenuation. Since the PV-panel takes lower conversion efficiency as T goes up, P_s and T show a negative correlation. Moreover, with the same R, T, and λ, P_s increases when the air visibility decreases. This is due to the attenuation of η_{bt} becomes higher with the air quality getting worse. To obtain the preferred battery charging power, P_s increases as η_{bt} attenuates.

Then, the corresponding consumed supplied energy during the charging procedure can be obtained as in Table V. It can be observed that, for the same beam wavelength, the consumed supplied power keeps the upward trend as T increases within certain radius under certain air quality. The ARBC system consumes much less supplied energy in all the listed scenarios for both 810 and 1550 nm compared with the RBC system.

Thereafter, for the same charging procedure, the supplied energy saved by the ARBC system compared with the RBC

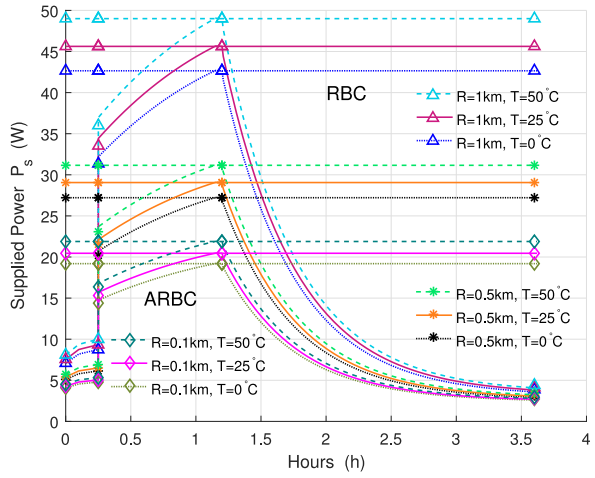

Fig. 17. Supplied power with different radius and temperature for 1550 nm (haze).

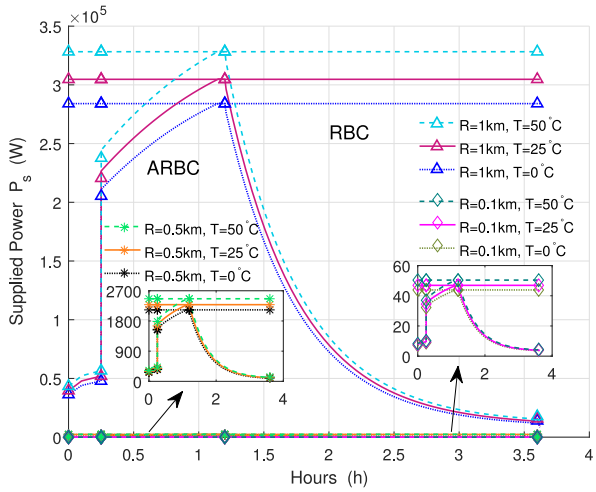

Fig. 18. Supplied power with different radius and temperature for 1550 nm (fog).

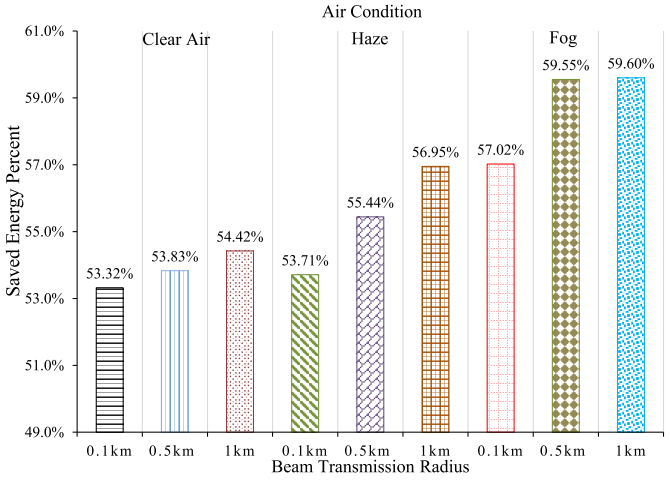

Fig. 19. Percent of saved supplied energy under 0 °C ($\lambda = 810$ nm).

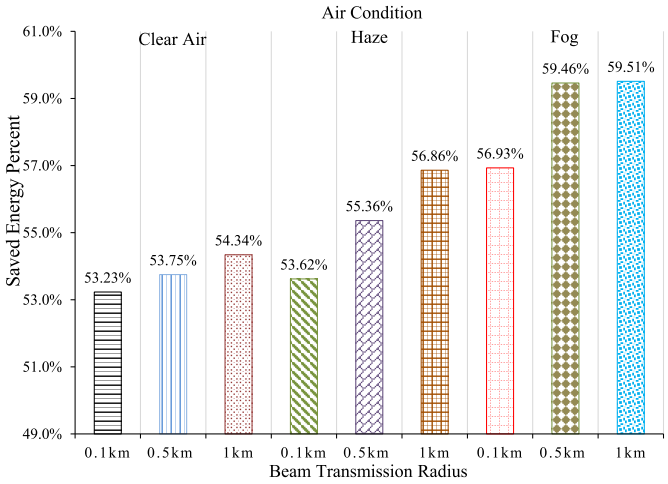

Fig. 20. Percent of saved supplied energy under 25 °C ($\lambda = 810$ nm).

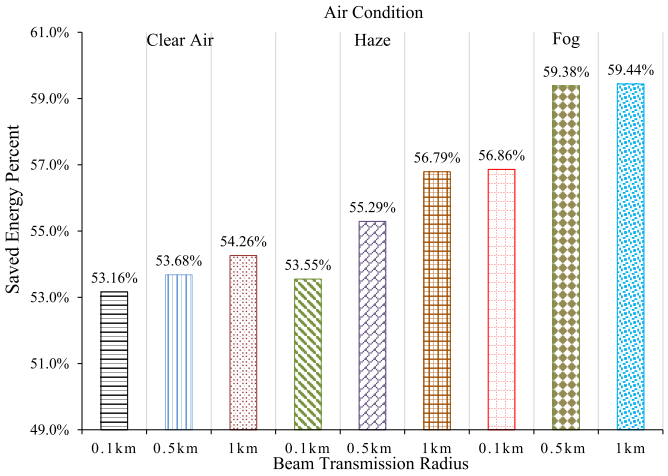

Fig. 21. Percent of saved supplied energy under 50 °C ($\lambda = 810$ nm).

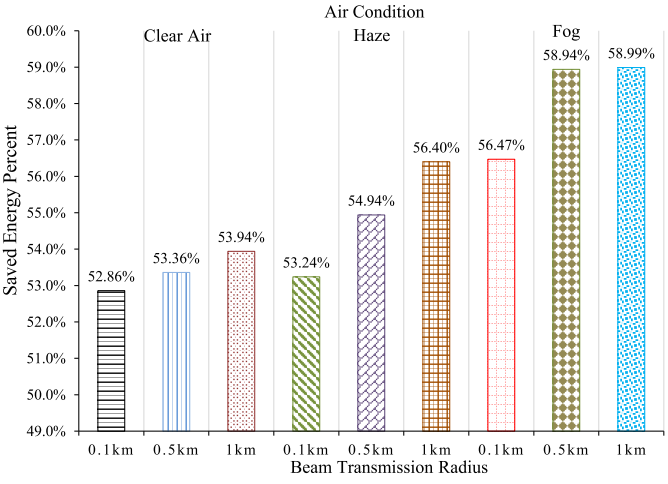

Fig. 22. Percent of saved supplied energy under 0 °C ($\lambda = 1550$ nm).

system can then be obtained. Figs. 19–21 show the saved supplied energy percentage for 810 nm under 0 °C, 25 °C, and 50 °C, respectively. Figs. 22–24 show the saved supplied energy percentage in the same scenarios for 1550 nm.

From Figs. 19–24, under the same air quality, the percentage of saved energy goes up with R increasing under the same T. With the same R and T, the percentage of saved energy goes up as the air quality declines. Since whether R increases

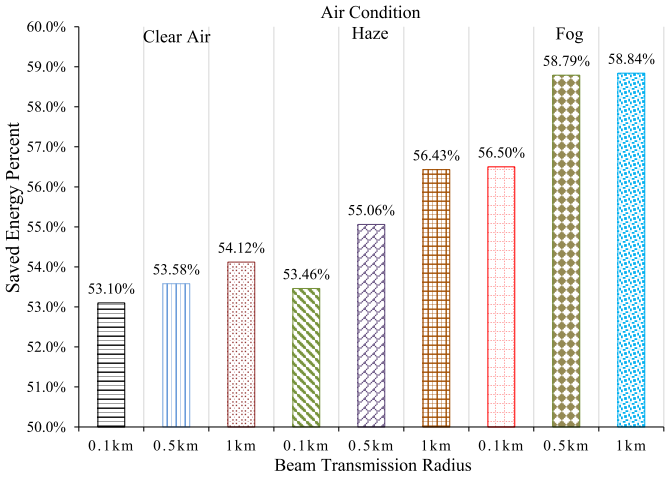

Fig. 23. Percent of saved supplied energy under 25 °C ($\lambda = 1550$ nm).

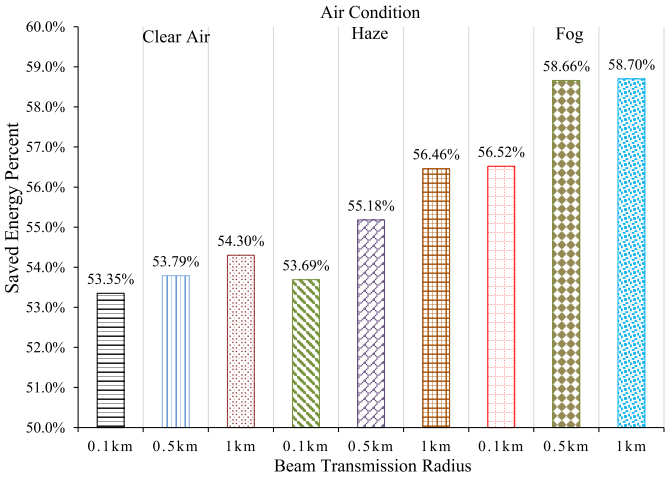

Fig. 24. Percent of saved supplied energy under 50 °C ($\lambda = 1550$ nm).

or air quality declines, η_{bt} decreases, and thus P_s needs to be increased. The increment of P_s leads to thermal effect and energy loss. Therefore, to obtain same battery charging power, the smaller P_s is preferred by ARBC compared with RBC. Hence, less energy will loss in the ARBC system, and more energy will be saved. This validates that the necessity of adopting the ARBC system increases as the preferred supplied power P_s rising. Moreover, in the above scenarios, 53%–60% supplied energy can be saved by the ARBC system no matter for the 810 nm or the 1550 nm system.

C. Summary

The ARBC mechanism introduced in Section III is numerically evaluated. Based on the end-to-end power conversion analysis, we quantitatively demonstrate the variation of the supplied power during battery charging period procedure. The supplied power depends on the PV-cell temperature, beam transmission efficiency, and beam wavelength. Furthermore, we obtain the battery charging energy and the supplied energy saved by the ARBC system compared with the RBC system in different scenarios.

The observations from the above analysis include the following.

1) With the increment of either the transmission radius R or the PV-cell temperature T, the preferred supplied power P_s takes an upward trend in the ARBC system.
2) The supplied power P_s shows a negative correlation with the air quality. That is, to say, with the improvement of the air quality, i.e., the enhancement of the visibility, less supplied power is required to get the certain battery charging power.
3) For the same air quality and transmission radius R, the consumed supplied energy goes up with the PV-cell temperature T increasing for the RBC system and the ARBC system.
4) For the same air quality, the percentage of the ARBC system saved energy goes up as the transmission radius R increases.
5) For the same transmission radius R, the ARBC system saves more energy with the air quality going down.
6) For battery charging, 61% energy can be saved by the ARBC system compared with the RBC system.
7) For the power supply, 53%–60% supplied energy is saved by the ARBC system compared with the RBC system.

V. Conclusion

An ARBC system is introduced in this paper based on the RBC system. The system design and numerical analysis of the ARBC system are presented to optimize battery charging performance in terms of battery charging profile. Given the supplied power, the battery charging power is influenced by various factors, including beam wavelength, beam transmission efficiency and PV-cell temperature etc. Numerical analysis illustrates that 61% battery charging energy and 53%–60% supplied energy can be saved by the ARBC system compared with the RBC system.

Several issues in this area are worth of further research.

1) The analysis in this paper is under ideal assumptions. For example, the feedback and measurement errors are inevitable in the practical system, which should be considered in the future.
2) For different beam wavelengths, the saved energy varies as the PV-cell temperature changing.
3) Different battery types have different battery charging profiles. Therefore, studying their impacts on ARBC is one of the future research areas.

Acknowledgment

The authors would like to thank the editors and the anonymous reviewers. The authors would like to thank colleagues in their laboratory. The authors would also like to thank H. Deng and M. Liu for their valuable suggestions, and A. Wu for polishing the figures.

References

[1] Q. Wu *et al.*, "Cognitive Internet of Things: A new paradigm beyond connection," *IEEE Internet Things J.*, vol. 1, no. 2, pp. 129–143, Apr. 2014.

[2] S. Stanković, I. Orović, and E. Sejdić, *Multimedia Signals and Systems*, 2nd ed. New York, NY, USA: Springer, 2016.
[3] S. Peng, S. Yu, and A. Yang, "Smartphone malware and its propagation modeling: A survey," *IEEE Commun. Surveys Tuts.*, vol. 16, no. 2, pp. 925–941, 2nd Quart., 2014.
[4] J. M. Fernandez and J. A. Borras, "Contactless battery charger with wireless control link," U.S. Patent 5 668 842, Feb. 2001.
[5] A. Esser and H.-C. Skudelny, "A new approach to power supplies for robots," *IEEE Trans. Ind. Appl.*, vol. 27, no. 5, pp. 872–875, Sep./Oct. 1991.
[6] J. Hirai, T.-W. Kim, and A. Kawamur, "Wireless transmission of power and information and information for cableless linear motor drive," *IEEE Trans. Power Electron.*, vol. 15, no. 1, pp. 21–27, Jan. 2000.
[7] S. E. Sarma, S. A. Weis, and D. W. Engels, "RFID systems and security and privacy implications," in *Proc. Int. Workshop Cryptograph. Hardw. Embedded Syst.*, Feb. 2003, pp. 454–469.
[8] A. Kurs *et al.*, "Wireless power transfer via strongly coupled magnetic resonances," *Science*, vol. 317, no. 5834, pp. 83–86, Jul. 2007.
[9] W. G. Bigelow, J. C. Callaghan, and J. A. Hopps, "General hypothermia for experimental intracardiac surgery; the use of electrophrenic respirations, an artificial pacemaker for cardiac standstill and radiofrequency rewarming in general hypothermia," *Ann. Surg.*, vol. 132, no. 3, pp. 531–539, Sep. 1950.
[10] D.-U. Bartsch, I. K. Muftuoglu, and W. R. Freeman, "Laser pointers revisited editorial," *Retina*, vol. 36, no. 9, pp. 1611–1613, Sep. 2016.
[11] R. Della-Pergola, O. Alpert, O. Nahmias, and V. Vaisleib, "Spatially distributed laser resonator," Israel Patent 20 140 126 603, May 2014.
[12] B. Feng, H. Zhang, H. Zhou, and S. Yu, "Locator/Identifier split networking: A promising future Internet architecture," *IEEE Commun. Surveys Tuts.*, vol. 19, no. 4, pp. 2927–2948, 4th Quart., 2017.
[13] Q. Liu *et al.*, "Charging unplugged: Will distributed laser charging for mobile wireless power transfer work?" *IEEE Veh. Technol. Mag.*, vol. 11, no. 4, pp. 36–45, Dec. 2016.
[14] Q. Zhang *et al.*, "Adaptive distributed laser charging for efficient wireless power transfer," in *Proc. IEEE 86th Veh. Technol. Conf. (VTC-Fall)*, Toronto, ON, Canada, Sep. 2017, pp. 1–5.
[15] Q. Zhang *et al.*, "Distributed laser charging: A wireless power transfer approach," *IEEE Internet Things J.*, to be published, doi: 10.1109/JIOT.2018.2851070.
[16] W. Fang, Q. Zhang, Q. Liu, J. Wu, and P. Xia, "Fair scheduling in resonant beam charging for IoT devices," *IEEE Internet Things J.*, to be published, doi: 10.1109/JIOT.2018.2853546.
[17] J. B. Goodenough and K. S. Park, "The Li-ion rechargeable battery: A perspective," *J. Amer. Chem. Soc.*, vol. 135, no. 4, pp. 1167–1176, Jan. 2013.
[18] W. Shen, T. T. Vo, and A. Kapoor, "Charging algorithms of lithium-ion batteries: An overview," in *Proc. 7th IEEE Conf. Ind. Electron. Appl. (ICIEA)*, Singapore, Jul. 2012, pp. 1567–1572.
[19] B. V. Zeghbroeck, *Principles of Semiconductor Devices*, 1st ed. Oxford, U.K.: Oxford Univ. Press, 2004.
[20] S. A. Salman, J. M. Khalel, and W. H. Abas, "Attenuation of infrared laser beam propagation in the atmosphere," *Diala J.*, vol. 36, pp. 2–9, 2009.
[21] J.-M. Liu, "Semiconductor lasers and light emitting diodes," in *Photonic Devices*, 1st ed. Cambridge, U.K.: Cambridge Univ. Press, 2005.
[22] M. Edouard and D. Njomo, "Mathematical modeling and digital simulation of PV solar panel using MATLAB software," *Int. J. Emerg. Technol. Adv. Eng.*, vol. 3, no. 9, pp. 24–32, Sep. 2013.
[23] M. S. Aziz, S. Ahmad, I. Husnain, A. Hassan, and U. Saleem, "Simulation and experimental investigation of the characteristics of a PV-harvester under different conditions," in *Proc. Int. Conf. Energy Syst. Policies (ICESP)*, Islamabad, Pakistan, Nov. 2014, pp. 1–8.
[24] G. Ding, Q. Wu, N. Min, and G. Zhou, "Adaptive resource allocation in multi-user OFDM-based cognitive radio systems," in *Proc. Int. Conf. Wireless Commun. Signal Process.*, Nanjing, China, 2009, pp. 1–5.
[25] T. Cleveland, "Battery charger adapts to multiple chemistries," *Power Electron.*, vol. 34, no. 7, pp. 26–31, Jul. 2008.
[26] S. Dearborn, "Charging Li-ion batteries for maximum run times," *Power Electron. Technol.*, vol. 31, no. 4, pp. 40–49, Apr. 2005.
[27] Y.-S. Hwang, S.-C. Wang, F.-C. Yang, and J.-J. Chen, "New compact CMOS Li-ion battery charger using charge-pump technique for portable applications," *IEEE Trans. Circuits Syst. I, Reg. Papers*, vol. 54, no. 4, pp. 705–712, Apr. 2007.
[28] A. P. Dancy, R. Amirtharajah, and A. P. Chandrakasan, "High-efficiency multiple-output DC–DC conversion for low-voltage systems," *IEEE Trans. Very Large Scale Integr. (VLSI) Syst.*, vol. 8, no. 3, pp. 252–263, Jun. 2000.
[29] G. R. Walker and P. C. Sernia, "Cascaded DC–DC converter connection of photovoltaic modules," *IEEE Trans. Power Electron.*, vol. 19, no. 4, pp. 1130–1139, Jul. 2004.
[30] Laser Diode Source CM Technologies. (Jul. 2017). *Laser Diode Source—808 nm*. [Online]. Available: https://www.laserdiodesource.com/shop/808nm-25Watt-Laser-Diode-Module-BWT-Beijing
[31] Laser Diode Source Seminex. (Jul. 2017). *Laser Diode Source—1550 nm*. [Online]. Available: https://www.laserdiodesource.com/laser-diode-product-page/1470nm-1532nm-1550nm-50W-multi-chip-fiber-coupled-module-Seminex
[32] I. I. Kim, B. McArthur, and E. J. Korevaar, "Comparison of laser beam propagation at 785 nm and 1550 nm in fog and haze for optical wireless communications," in *Proc. Inf. Technol. Int. Soc. Opt. Photon.*, Boston, MA, USA, Feb. 2001, pp. 26–37.
[33] N. Femia, G. Petrone, G. Spagnuolo, and M. Vitelli, "Optimization of perturb and observe maximum power point tracking method," *IEEE Trans. Power Electron.*, vol. 20, no. 4, pp. 963–973, Jul. 2005.
[34] F. Z. Peng, F. Zhang, and Z. Qian, "A magnetic-less DC–DC converter for dual voltage automotive systems," *IEEE Trans. Ind. Appl.*, vol. 39, no. 2, pp. 511–518, Mar./Apr. 2003.

Qingqing Zhang (S'16) received the M.E. degree in computer science and technology from the Hunan University of Technology, Hunan, China, in 2016. She is currently pursuing the Ph.D. degree at the College of Electronics and Information Engineering, Tongji University, Shanghai, China.

Her current research interests include wireless charge, wireless power transfer, simultaneous wireless information and power transmission, Internet of Things, and communications.

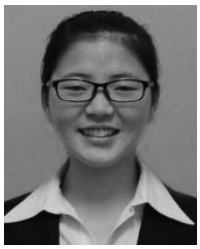

Wen Fang received the B.S. degree in computer science and technology from the Shandong University of Science and Technology, Qingdao, China, in 2017. She is currently pursuing the Ph.D. degree at the College of Electronics and Information Engineering, Tongji University, Shanghai, China.

Her current research interests include wireless power transmission, development of remote wireless charging technology, Internet of Things, and financial transactions.

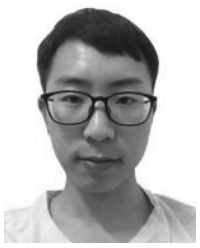

Mingliang Xiong received the B.S. degree in communication engineering from the Nanjing University of Posts and Telecommunications, Nanjing, China, in 2017. He is currently pursuing the Ph.D. degree at the College of Electronics and Information Engineering, Tongji University, Shanghai, China.

His current research interests include wireless power transfer, simultaneous wireless information and power transfer, and Internet of Things.

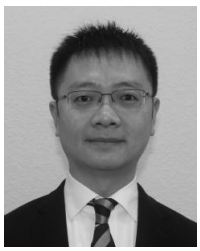

Qingwen Liu (M'07–SM'15) received the B.S. degree in electrical engineering and information science from the University of Science and Technology of China, Hefei, China, in 2001, and the M.S. and Ph.D. degrees from the Department of Electrical and Computer Engineering, University of Minnesota, Minneapolis, MN, USA, in 2003 and 2006, respectively.

He is currently a Professor with the College of Electronics and Information Engineering, Tongji University, Shanghai, China. His current research interests include wireless power transfer and Internet of Things.

Jun Wu (M'03–SM'14) received the B.S. degree in information engineering and M.S. degree in communication and electronic systems from Xidian University, Xian, China, in 1993 and 1996, respectively, and the Ph.D. degree in signal and information processing from the Beijing University of Posts and Telecommunications, Beijing, China, in 1999.

He was a Principal Scientist with Huawei, Shenzhen, China, and Broadcom, Irvine, CA, USA. In 2010, he joined the College of Electronics and Information Engineering, Tongji University, Shanghai, China, as a Professor. His current research interests include wireless communication, information theory, and multimedia signal processing.

Pengfei Xia received the Ph.D. degree from the Department of Electrical and Computer Engineering, University of Minnesota, Twin Cities, MN, USA, in 2005.

He is currently a Full Chair Professor with the College of Electronics and Information, Tongji University, Shanghai, China. He is a Co-Editor of *60 GHz Technology for Gb/s WLAN and WPAN: From Theory to Practice* (Wiley, 2011). His current research interests include wireless communications, networks, and signal processing.

Dr. Xia was a co-recipient of the IEEE Signal Processing Society Best Paper Award in 2011. He is currently serves as a Signal Processing for Communications (SPCOM) Technical Committee member and SPCOM Industrial/Government Subcommittee Chair for the IEEE Signal Processing Society.